Materials Horizons

ROYAL SOCIETY OF CHEMISTRY

COMMUNICATION

View Article Online
View Journal | View Issue

Cite this: *Mater. Horiz.*, 2021, 8, 1570

Received 2nd January 2021,
Accepted 11th March 2021

DOI: 10.1039/d1mh00006c

rsc.li/materials-horizons

The pursuit of stability in halide perovskites: the monovalent cation and the key for surface and bulk self-healing†

D. R. Ceratti, *[a] A. V. Cohen,[a] R. Tenne,[b] Y. Rakita,[a] L. Snarski,[a] N. P. Jasti,[cd] L. Cremonesi, [e] R. Cohen,[c] M. Weitman,[c] I. Rosenhek-Goldian,[f] I. Kaplan-Ashiri,[f] T. Bendikov,[f] V. Kalchenko,[g] M. Elbaum,[h] M. A. C. Potenza,[e] L. Kronik, *[a] G. Hodes*[a] and D. Cahen *[acd]

We find significant differences between degradation and healing at the surface or in the bulk for each of the different $APbBr_3$ single crystals (A = $CH_3NH_3^+$, methylammonium (MA); $HC(NH_2)_2^+$, formamidinium (FA); and cesium, Cs^+). Using 1- and 2-photon microscopy and photobleaching we conclude that kinetics dominate the surface and thermodynamics the bulk stability. Fluorescence-lifetime imaging microscopy, as well as results from several other methods, relate the (damaged) state of the halide perovskite (HaP) after photobleaching to its modified optical and electronic properties. The A cation type strongly influences both the kinetics and the thermodynamics of recovery and degradation: FA heals best the bulk material with faster self-healing; Cs^+ protects the surface best, being the least volatile of the A cations and possibly through O-passivation; MA passivates defects *via* methylamine from photo-dissociation, which binds to Pb^{2+}. DFT simulations provide insight into the passivating role of MA, and also indicate the importance of the Br_3^- defect as well as predicts its stability. The occurrence and rate of self-healing are suggested to explain the low effective defect density in the HaPs and through this, their excellent performance. These results rationalize the use of mixed A-cation materials for optimizing both solar cell stability and overall performance of HaP-based devices, and provide a basis for designing new HaP variants.

New concepts

Studying photo-damage in and on halide perovskites, HaPs, we show how, after being damaged, the material heals much more readily in confined chemical environments than if products of the damage can escape, or can further react with the ambient. This finding is especially important because current encapsulation strategies of HaP-based devices do not take this into account and use materials that can react with damage products, thus interfering with self-healing. Building on our earlier discovery of HaP self-healing, we now define the reactions and conditions necessary for the process. We show and explain differences between the monovalent methylammonium, formamidinium and cesium cations for damaging and self-healing in-bulk and on-surface of these perovskites. This work underlines the relevance of the dynamic nature of HaPs, materials in a steady-state of damage and repair, determined by both the kinetics and thermodynamics of the critical reactions identified here. On this basis, we can now explain the contribution of each monovalent cation to the overall stability and quality of mixed cation perovskites in record efficiency solar cells. Finally we show that the materials' self-healing is crucial for the properties of devices because self-healing is critical in determining the low defect densities of the HaPs.

1 Introduction

1.1 Background

Halide Perovskites (HaPs) continue to have significant impact on the field of solar cells, thanks to their very low cost, ease of production, and competitive efficiencies that are comparable, if not superior, to those of established photovoltaic (PV) technologies.[1–3] In the wake of these PV results, other applications, such as light-emission, radiation detection, and electronics are explored.[4–7] Despite all these efforts, a critical issue hangs as a sword of Damocles over the entire field: stability. Various approaches for delaying or avoiding device degradation, due to external influences such as heat, light, or chemicals, have been tested.[8] Encapsulation of the solar cell and perovskite passivation through long alkylamine molecules,[9] as well as use of 2D variants of HaPs,[10,11] show promise for avoiding degradation;

[a] *Weizmann Institute of Science, Department of Materials and Interfaces, 7610001, Rehovot, Israel. E-mail: davide-raffaele.ceratti@weizmann.ac.il, david.cahen@weizmann.ac.il, gary.hodes@weizmann.ac.il, leeor.kronik@weizmann.ac.il*
[b] *Weizmann Institute of Science, Department of Physics of Complex Systems, 7610001, Rehovot, Israel*
[c] *Bar Ilan University, Department of Chemistry, 5290002, Ramat Gan, Israel*
[d] *Bar Ilan University, Bar-Ilan Institute for Adv. Mater., BINA, 5290002, Ramat Gan, Israel*
[e] *Department of Physics and CIMAINA, University of Milan, via Celoria, 16, 20133, Milan, Italy*
[f] *Weizmann Institute of Science, Department of Chemical Research Support, 7610001, Rehovot, Israel*
[g] *Weizmann Institute of Science, Department of Veterinary Resources, 7610001, Rehovot, Israel*
[h] *Weizmann Institute of Science, Department of Chemical and Biological Physics, 7610001, Rehovot, Israel*

† Electronic supplementary information (ESI) available. See DOI: 10.1039/d1mh00006c

still, the need for decades of stable operation (at least for use in solar cells) under realistic conditions makes the question of the intrinsic stability of the materials themselves crucial. Hereafter we use the term "intrinsic stability" for the stability of the material, irrespective of external (ambient, light, temperature) influence. This can be tested by stressing the material to different extents; intrinsically unstable (or metastable) materials will degrade already with low intensity stresses.

Degradation pathways have been identified for the thermal and photo-decomposition of methylammonium (MA) lead halides using mass spectroscopy[12] and STA-FTIR (simultaneous thermal analysis (STA) and Fourier Transform-Infrared (FT-IR) Spectroscopy).[13] The pathways that were identified involve the release of methylamine, hydrogen halides, halomethanes, ammonia, and halogens and likely cause loss of photo-conversion efficiency. However, such mechanistic analysis is lacking for formamidinium (FA) and cesium (Cs) lead halides, which are critical building blocks of the currently most-efficient halide perovskite solar cells.[2,14] Furthermore, an important question then follows: are decomposition mechanisms connected to an intrinsic material instability or are there ways to avoid or eliminate them, or heal the damage? For example, mechanisms involving the attack of the material by external chemicals are strongly inhibited by encapsulation and do not affect the intrinsic material stability. However, if there are readily accessible degradation pathways that do not involve external chemicals, HaPs would be practically unusable for long-term operation, unless...the material can self-heal. To address this question, we focus our study on the perovskites themselves. While studies on complete cells are the most relevant ones for applications, using multi-component samples makes determining the limits of stability of the HaP material, the one irreplaceable element of a perovskite solar cell, very difficult and practically impossible.

1.2 Approach

We assess the fundamental differences between the stability of the bulk (chemically inaccessible) and surface (chemically relatively accessible) of HaP single crystals (SI.1, ESI†), by monitoring healing from strong, supra-band-gap illumination-induced damage (SI.2 and SI.3, ESI†), focusing on the critical role of A cations in HaP stability.

1.3 Summary of findings

(1) There are very significant differences between self-healing of perovskites[15,16] in the bulk and that at surfaces, with major effects on the perceived stability of the material.

(2) Upon illumination the optoelectronic properties of the materials change differently at the surface and in the bulk, including whether and how they revert to the original state after photo-damage, as shown through confocal, and fluorescence lifetime imaging microscopy (FLIM).

To pinpoint the chemical origin of these variations,

• We analyze the effect of photodamage at the surface and in the near-surface region.

• We use density functional theory (DFT) simulations to rationalize, at a molecular level, the A cation effect. In particular, we discuss how the self-healing directly controls the defect density in the HaPs.

We conclude that.

(3) the thermodynamically-determined stability and defect density in the bulk are the relevant quantities for solar energy applications.

(4) Surface degradation is more pronounced than bulk degradation, due to kinetic effects (material loss), which can be hindered with tailored encapsulation and judicious electron transporting layer (ETL) and hole transporting layer (HTL).[17]

(5) We identify and explain the mechanisms involved in the self-healing, an obvious step towards optimizing self-healing. This result constitutes a major step beyond the conclusion of our earlier work, *i.e.*, that bromide perovskite can self-heal.[15]

Thus, our results also go well beyond earlier suggested, deduced, or assumed self-healing,[18–22] and pave a way to reach long-term stable halide perovskite solar cells rationally, *i.e.*, beyond doing so primarily empirically.

2 Results: PL effects of surface and bulk self-healing

2.1 Time dependence of photoluminescence (PL) intensity

2.1.1 Methodology. The PL of HaPs after photodamage is assessed using an experiment that is, essentially, one of fluorescence recovery after photobleaching (FRAP), which is of common use in biological experiments involving fluorophores (see ESI,† SI.2 and SI.3). For the bulk, we use a protocol described elsewhere.[15] For the surface, we use a variant of the same method to assess the (near)surface damage and recovery of the $APbBr_3$ single crystals (see ESI,† SI.3 for the procedure). Clearly, photodamage can be performed at different intensities of light. It is important to assess damages that are effectively inflicted by the sun during normal operation of a solar cell. We therefore evaluated the amount of energy that our procedure releases in the system taking into account the dwell time of each bleaching cycles (8 μs and 9.97 μs for 1P and 2P respectively). We tuned the power of the lasers to release an amount of energy equivalent to the one that the sun releases in seconds. For a detailed description of the energy absorbed by the material refer to SI.4 and SI.5 (ESI†). We also assessed the variations of temperature (SI.6, ESI†) expected in the material due to the laser illumination, used to cause damage. Based on the known values of absorption coefficients,[23] of photo-generated carrier diffusion length (which can reach micrometers[24]), heat conductivity,[25] and heat capacity,[26] we derive a temperature variation of <1 K, *i.e.*, below the ambient temperature control during the experiment, and too small to lead to heat-induced damage.

For the sake of discussion, we can ask if self-healing of damage due to larger (than 1 K) temperature changes will occur. Because the halide perovskite chemistry is relatively simple (see Section 5 of this article), there is only a limited number of possible degradation products and, actually, all form whatever the origin of the damage. Even if the ratios of the amount of these will differ between light- and heat-induced

damage, self-healing will occur, whatever the origin of the damage. Since damage can heal completely (*cf.* next paragraph) we deduce that each decomposition product will be part of the healing process, irrespective of the decomposition pathway that it originates from. The exception to this discussion is the case of $PbBr_2$, which photolyzes[27,28] to Pb^0 and Br_2, while thermally it does not decompose (rather, it evaporates). For the latter it was argued that temperature is critical for long-term PCE stability.[29,30]

2.1.2 Overview of PL intensity changes. In Fig. 1, we report the background-normalized PL just after bleaching (solid lines) and after recovery (dashed lines) as a function of the laser power (LP), given as a percentage of the full LP, which is 880 μW for 1P at 488 nm and 771 mW for 2P at 800 nm. For all samples, the most striking feature is that we detect a sharp, sample-dependent threshold for damage in the 1P-surface experiment, but not in the 2P-bulk one. In the latter, the effects of photo-bleaching are more gradual (note that for 2P (1P) bleaching, the deposited energies grow quadratically (linearly), with the % of LP).

2.1.3 Photodamage on the surface. At the surface, $MAPbBr_3$ crystals appear to be the most resistant to photo-damage: with 1P-surface excitation, the LP needs to reach 60% of its maximal value whereas for FA and Cs 45–50% suffices. However, once damaged, the MA material heals only slightly (PL recovers 15% of its original value), in contrast to FA and Cs based samples, which show partial to almost complete healing after 12 h. For 1-LP $>80\%$ the Cs HaP surface even shows increased PL

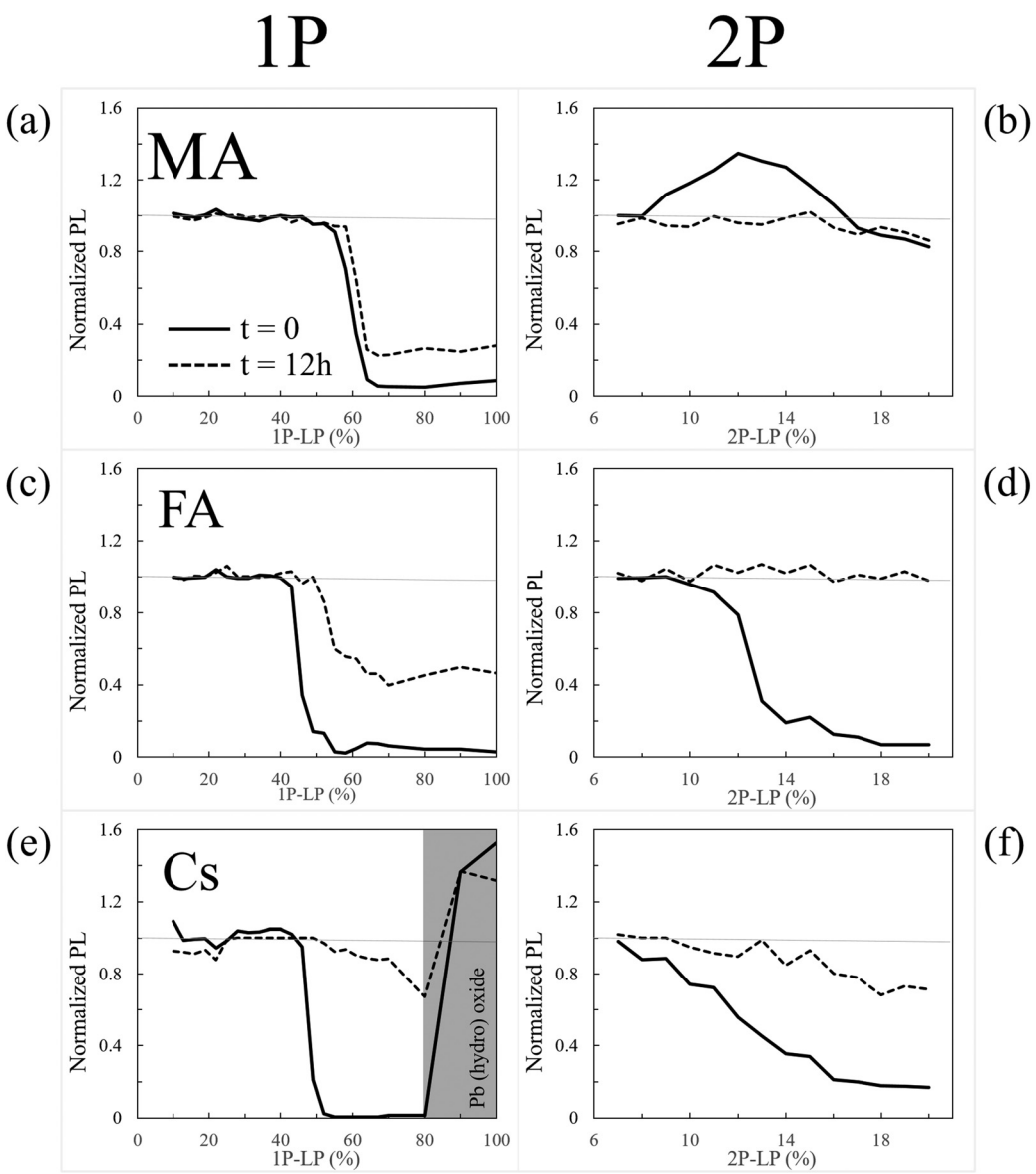

Fig. 1 Background-normalized PL intensity of (a and b) MA, (c and d) FA, and (e and f) Cs lead tribromide perovskite samples, at time zero, $t = 0$, *i.e.*, immediately after bleaching) (—) and after 12 h of recovery, $t = 12$ h (- - -) for the 1P (left) and 2P (right) experiments. The laser power (LP) is expressed in %, with 100% (1P) being 880 μW and (2P) 771 mW. For Cs, we see in the 1P experiment a large PL increase exceeding the initial level at $>80\%$ LP as marked by the gray shading. This corresponds to a new, blue-shifted phase discussed in the text.

intensity compared to the pre-bleaching and background PL. Surface behavior can be influenced, usually negatively, by pre-existing surface defects that are known to influence the chemical reactivity and the stability of HaPs.[25,26] Detecting and measuring the surface defect effects on self-healing, even if not yet possible today, will constitute a major step in stabilizing polycrystalline thin HaP films.

2.1.4 Photodamage in the bulk. Analyzing the damage by 2P-bulk excitation, we see that the increase in damage always gradually increases with 2P-LP. Self-healing is more effective with an organic A cation (Fig. 1b and d) than with Cs (Fig. 1f). In particular, MA is subject to two processes after photobleaching: (1) for low to medium LP (with energies equivalent to 30–50 seconds of normal sun irradiation) the process increases the PL compared to the pre-bleaching and background PL; (2) for high LP (50–80 seconds of sun irradiation) the process decreases PL intensity. After bleaching, the system reverts to the original state for both processes. Process (1) requires recovery times of $\sim$30 s while process (2) requires several minutes. FA and Cs samples show a single process similar to process (2) of MA. After the bleaching, FA heals completely and very rapidly ($<$30 s). For low 2P-LP the healing is so rapid that the PL is already partially recovered within the time that elapses between the end of the 2P excitation and the PL measurement of the first data-point (5 seconds). Cs HaP, however, is healed on much longer timescales ($>$12 h).

2.1.5 Damage time scale: transient *vs.* steady-state. We stress that even though our results are valid for a mechanism that takes place after a short pulse of irradiation, they are critical also for long-term operation, because the mechanism is always present in the material, meaning these damage and healing processes are continuous! As long as the time scale of healing is short enough to prevent damage accumulation, self-healing can influence the material properties, also for extremely long times of exposure to the damage-causing factor. Comparable examples are Si:Li, used in commercial radiation detectors, and CIGS, used in commercial solar cells.[31]

2.2 PL spectroscopy

PL spectroscopy can indicate modification of material composition and/or structure that is damage/healing-induced, beyond changes in PL intensity.

2.2.1 Methodology. Fig. 2a shows PL emission spectra recorded for the three samples, after bleaching through 2P excitation (for experimental settings see SI.3, ESI†). Bleaching was performed at the surface, with the exception of MA with medium intensity that was bleached slightly inside ($\sim$2.5 μm) the crystal. The spectra were recorded using 2P excitation at/near the surface because of three reasons: (1) using 2P excitation, all collected PL reaches the detector, thus avoiding any filtering which would be necessary to eliminate the 1P exciting light. The collected spectra are then more reliable than for a 1P measurement; (2) 2P excitation in the (semi)bulk is the only way to modify MA to its transient, more PL intense, state. Note that focusing the 2P light precisely at the surface requires extreme attention as slight inclination of the sample can shift the behavior from surface-like to bulk-like; (3) spectra from the bulk ($\sim$110 μm) are modified by self-absorption effects. Photons emitted from the bulk pass through the material, which absorbs more efficiently the higher energy photons. As a result, the PL peak from the bulk is blue-filtered and any true blue-shift due to chemical or structural variations is masked. Focusing on the surface with a 2-photon excitation, we excite the carriers in a volume that reaches deeper into the material ($\sim$1.5 μm) than what one would obtain with 1P excitation ($\sim$0.2 μm). As we discussed earlier, the excited carriers diffuse, therefore a slight larger volume emits PL after 2P excitation on the surface. As the diffusion length of the carriers is larger than the focus of the objective through which PL is collected, this effect should not modify the recorded spectra significantly.

2.2.2 Photodamage-induced spectral shifts. Analyzing Fig. 2a, we find that neither the more luminescent nor the less luminescent form of $MAPbBr_3$ shows a detectable PL peak shift (Fig. 2a-MA). Similarly, there is no significant shift of the $FAPbBr_3$ PL peak (note that absolute PL values are reported in Fig. 2). In the same way, $CsPbBr_3$ shows no change in the PL emission spectrum as a result of reversible bleaching ('medium' in the figure). However, it does show a 6 nm blue shift for areas which exhibit increased PL intensity after bleaching with the highest LP (Fig. 2a, Cs-High).

2.2.3 Chemical implications. The blue shift after the photobleaching of $CsPbBr_3$ on the surface can be attributed either to the formation of lead (hydro)oxide[32,33] or carbonate[34,35] or to the oxygen-related sequestration of Pb^{2+} from the crystal lattice, leaving a Cs-rich material. In the latter case, the blue shift can arise from a contribution by Cs_4PbBr_6, known to emit at shorter wavelength (500 nm) than $CsPbBr_3$ (530 nm).[36] A Pb-deficient perovskite composition, which would agree with our PL emission data, has been reported,[37] showing how variations in composition blue-shift the PL peak. For completeness, we report that spectra recorded completely in the bulk do not show any peak shift either for the three materials.

2.3 PL lifetime imaging (fluorescence lifetime imaging microscopy, FLIM)

The absence of spectral shifts in the perovskite emission leaves the possibility that bleaching influences the material through thermal or photo-induced trap formation. To explore this, we map the PL lifetime of the perovskite crystals both at the surface and in the bulk.

2.3.1 Expected effect of the traps. Bleaching-created traps should decrease the lifetime of the photo-generated carriers and decrease PL lifetime. Decreasing the lifetime also decreases the PL intensity, specifically through thermal or photo-induced trap formation. To explore this, we map the PL lifetime of the perovskite crystals both at the surface and in the bulk.

Bleaching-created traps should decrease the lifetime of the photo-generated carriers and decrease PL lifetime. Decreasing the lifetime also decreases the PL intensity. Specifically, in a trap-assisted recombination regime (indicated by exponential decay of the instantaneous PL intensity over time), the integrated PL intensity between pulses decreases if the lifetime decreases.

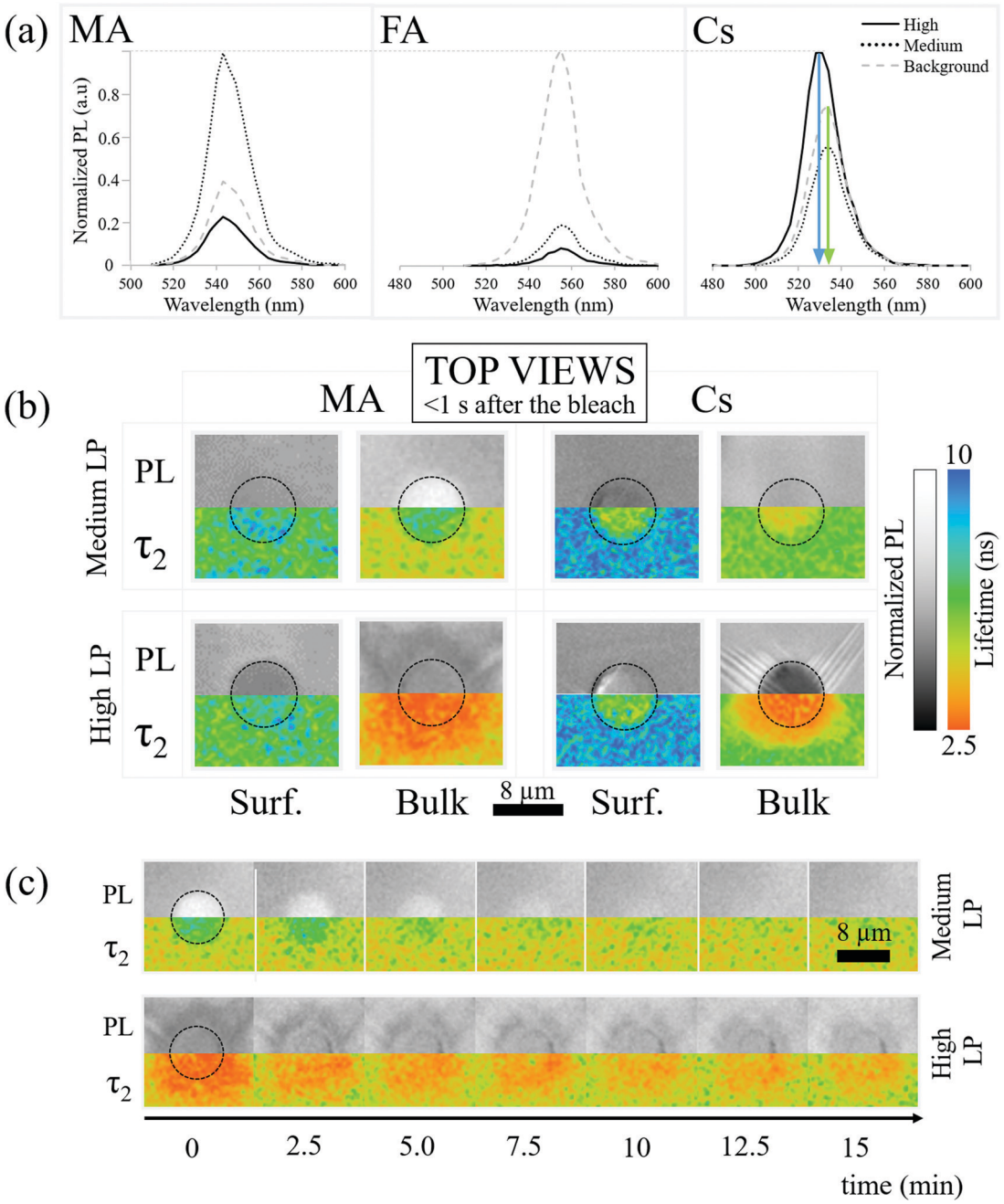

Fig. 2 (a) Normalized PL spectra (the value of 1 is set for strongest PL after the bleaching cycle) from the surfaces of MA-, FA- and Cs-$PbBr_3$. —: strongest bleaching. . . .: medium bleach. - - -: background (at 20 μm lateral distance from the ~8 μm diameter bleached area). The arrows in the spectra of the Cs samples emphasize the blue shift of the PL peak for the high LP bleach (blue arrow), with respect to the PL peaks of the background or medium LP bleach (green arrow). The spectra are normalized to the maximum PL value of each experiment. Medium bleach in the MA case is recorded from slightly (1 μm) inside the single crystal. In all other cases it is recorded on the surface. (b) (Mirrored) images of the PL intensities (grayscale) and of PL lifetimes (color-coded – right-most legend) for the same areas/regions of the MA and Cs samples on the surface and in the bulk, just after (<1 s) medium and strong bleaching. (c) As (b) for only the MA sample and only in the bulk, showing the time evolution of the PL (grayscale) and PL lifetime after bleaching, at medium LP (top) and high LP (bottom). Each step corresponds to a delay of 2.5 minutes. As in (b) the PL and lifetime images are mirrored to facilitate comparison between them.

In Fig. 2b we relate the PL intensities (top) and FLIM (bottom) measurements of the MA and Cs samples just after medium LP (30 seconds of solar illumination) and high LP (100–200 seconds of solar illumination) bleaching on the surface and in the bulk (110 μm). When discussing PL intensities we consider the PL "increased"/"decreased" if it is more/less intense than the background respectively.

The PL decay is found to be bi-exponential (details of the fitting are given in SI.7, ESI†). Following SI.7 (ESI†), the fastest decay is due to carrier trapping and the slowest to detrapping.

We focus on the slowest decay because it is the kinetically limiting process. Additional information on the shorter lifetime results/processes is reported in SI.7 (ESI†).

2.3.2 Results: FA. Data for the FA samples are not reported because the lifetime of the photogenerated carriers is of the order of the time delay between the laser pulses (12.5 ns), or longer, which does not allow a proper fit of the decay.

2.3.3 Results: MA, effect of bleaching on the lifetime. Fig. 2b-MA-Surface shows that the PL intensity decreases (darker semi-circle, top half) at the surface for both medium and high LP. This decrease is not accompanied by any clear variation in the PL lifetime between the exposed (inside the dotted circle) and non-exposed (outside the circle) volumes.

Fig. 2b-MA-Bulk shows an increase of lifetime for medium LP compared to the pre-bleaching and background lifetime (Fig. 2b-MA-Bulk, top), where the PL increases, along with a decrease of the lifetime for high LP (Fig. 2b-MA-Bulk, bottom), where the PL intensity decreases. Note that the lifetime of the carriers emitted from unbleached parts of the material (background of image Fig. 2b-MA-Bulk) changes between the surface ($\sim$6.5 ns) and the bulk ($\sim$5 ns).

2.3.4 Causes: MA, effect of bleaching on the lifetime. Before discussing the effect of the bleaching, we briefly note 2 possible causes for the different values of the PL lifetime between the surface and the bulk:

(1) Solvent molecules (γ-ButyroLactone (GBL), DiMethylFormamide (DMF) and/or DiMethyl SulfOxide (DMSO)) that can interact strongly[38] with the Pb^{2+} ions are incorporated into the HaP crystals as defects and can act as recombination centers, thus reducing the lifetime. Mass spectroscopy shows that GBL, DMF and/or DMSO molecules are present in the single crystals (*cf.* SI.8, ESI†). Ref. 39 shows tail states in high-resolution photoemission spectroscopy, if DMSO is used in HaP film preparation. The assumption in this explanation is that solvent molecules are readily removed from the surface by evaporation, but remain trapped in the bulk.

(2) The density of shallow defects at/near the surface that can trap (minority) carriers is high enough so that less carriers actually recombine per unit time, increasing the measured carrier lifetime; the trapped carriers will eventually de-trap and recombine *via* band-to-band transitions. Such effects are known for other bulk semiconductors.[40]

(Dis)proving these hypotheses needs work that is beyond the scope of the present study.

For what concerns the effect of photobleaching, we interpret the observations showed in Fig. 2b-MA-Surface as a ''shadowing'' effect due to a non-emitting material formed on the surface. This material blocks the PL originating from the $MAPbBr_3$ lying below it. In addition, the microscope assesses the material up to a depth of $\sim$1 μm, even if focused on the surface. If complete degradation happens at or very close to the surface (within $\sim$100 nm), the overall PL also decreases because the amount of emitting material decreases. Because the degraded material does not emit light, the photons emitted from deeper in the crystal will be the result of the recombination of carriers, with the lifetime typical for the undamaged material. Importantly, this result supports the observation that simply monitoring the lifetime is not sufficient for determining the quality of a material, a conclusion that we drew also earlier, based on other data.[41]

As to the bulk, what is observed in Fig. 2b-MA-Bulk follows what is expected from a decrease/increase of trap density which both increase/decrease the PL intensity and PL lifetime. The chemical origins of this effect cannot be simply extrapolated from these observations and constitute the subject of a subsequent section.

2.3.5 Results: Cs, effect of bleaching on the lifetime. For the Cs sample we observe a reduction of PL lifetime of the background from $\sim$10 ns at the surface to $\sim$7 ns in the bulk. Bleaching always causes a reduction of the lifetime. For completeness, we also report the observed values of lifetime for the more photo-luminescent, blue-shifted material obtained by bleaching the Cs sample at the surface with high LP. Fig. 2b-Cs-Surface-High LP shows a reduction of the PL lifetime from 8–10 ns in the unbleached crystal to $\sim$5.5 ns.

2.3.6 Causes: Cs, effect of bleaching on the lifetime. To explain the difference in PL lifetime between the surface and bulk in the Cs crystal, the solvent-related cause (option (1) above) seems even more probable. $CsPbBr_3$ crystals are grown in a DMSO solution and DMSO–Pb^{2+} complexes are known to form in solution and to crystallize in the presence of inorganic anions.[42] Also, DMSO is found in Cs-containing crystals by mass spectroscopy (see SI.8, ESI†).

The effect of the bleaching follows what is expected at the surface for medium LP and in the bulk (Fig. 2b-Cs), *i.e.*, bleaching reduces the lifetime. The PL intensity decreases because a larger number of carriers recombine through faster, non-radiative, processes. At the same time, the high LP Cs-Surface data show an opposite trend with an increase of PL intensity despite a reduction in lifetime compared to the pre-bleaching state. This is probably due to the fact that the blue-shifted material has a higher PL quantum efficiency than the background PL of the perovskite.

2.3.7 Results: evolution of the PL lifetime during healing. As lifetime is proportional to the defect density in single defect models, simple PL can be used to follow the trap density over time. Given that we find that the PL self-healing decay is exponential, we can infer that a single (migrating) species is critical for the process. In Fig. 2c we compare PL and FLIM images of the MA sample at different times after photobleaching in the bulk, showing similar lifetime and PL intensity changes during the healing process. In Section 4 we provide data that suggest that the species may be a (complex) bromine interstitial (high-LP) or methylamine-associated (medium-LP).

2.4 Interim conclusions

We showed that in nearly all cases changes in PL intensity directly relate to PL lifetime changes. This suggests that both have a common cause, which could be a change of defect density. However, we found that equivalent laser irradiation treatments affect the MA-, FA-, and Cs-perovskites differently. Moreover, we showed in Section 2.1 that the A cation influences self-healing of the perovskites (*cf.* Fig. 1). This indicates that the A cation is key in determining the stability of the perovskite. This conclusion points to a chemical basis for the differences, given the lack of a direct effect of the A cation on the electronic

structure of the material.[43,44] We proceed to study these differences and try to understand their chemical origins, analyzing the surface experimentally (Section 3) and the bulk through DFT simulation (Section 4).

3 Results: characterization of surface damage

We used atomic force microscopy (AFM), scanning electron microscopy (SEM), energy-dispersive X-ray spectroscopy (EDS), and X-ray photoelectron spectroscopy (XPS) to characterize the (near-)surface damage and to investigate changes of morphology and composition after the bleaching cycles.

3.1 AFM

Fig. 2b-MA-surface-high LP shows that MA samples exhibit a slightly more luminescent halo up to several μm from the strongly bleached area. Because no bleaching was performed in that region and the heat of the bleaching does not significantly increase the temperature in and around the bleached material (*cf.* SI.6, ESI†), the modification of the PL has to originate from chemicals released upon bleaching of the surface. Fig. 3(a) shows AFM images of a sample surface after 100 consecutive bleaching cycles (at high LP) taken in an area, equivalent to the one showing a halo in Fig. 2b-MA-Surface-High LP. We used 100 cycles to increase the effect of the halo formation sufficiently, to allow measuring the bleaching effect up to one day after bleaching. Because the time delay between bleach cycles is 10 seconds, they can be viewed as separate events that inflict cumulative damage (see SI.6, ESI† for details). In this way the amount of material, released from the bleached spot, increases with consequent stronger effect on the region around that spot.

AFM imaging reveals the formation of small, possibly HaP particles (as the PL spectrum, not shown, remains that of $MAPbBr_3$). We suggest this is formed by the decomposition products, resulting from surface photochemical vaporization by the laser, that fall back on the sample (horizontally placed – laser is incident from the top) after cooling. However, we cannot be certain of their composition because the PL spectrum can originate from the underlying crystal. The AFM images in Fig. 3a were obtained 0.5 h (i) and 1 day (ii) after the 100 bleaching cycles of the area, around which a halo appeared. Increasing the number of bleaching cycles assists in locating the spot optically (Fig. S7, ESI†) and allows imaging of the halo area that formed away from the bleached area (details in SI.11, ESI†). Comparing Fig. 3a(i) and (ii), we infer that the material connecting the different particles, seen in (i), evaporates with time and is probably a viscous liquid, as suggested by its flattened shape and the issues with direct AFM imaging very near the bleached area (see SI.11, ESI†). We attribute the presence of this liquid to re-absorbed CH_3NH_2 and NH_3, known to dissolve into the $MAPbBr_3$ to form a viscous phase.[45] The other products of decomposition (HBr, CH_3Br) do not interact with the solid and would not form such a phase. Because the vapor pressure of NH_3 at 25 °C ($\sim$10 bar)[46] is higher than that of CH_3NH_2 ($\sim$2 bar),[47] which is consistent with their boiling points (NH_3: −33.3 °C;[48] CH_3NH_2: 6 °C[49]), we expect CH_3NH_2 to dominate absorption after vaporization. This argument can explain why we do not find any PL halo around bleached areas on FA and Cs samples: their decomposition products cannot form such a liquid with the corresponding HaP.

3.2 SEM

Fig. 3b shows SEM images of the surfaces of MA, FA and Cs after 100 bleaching cycles. As in the case of Fig. 3a, the repetition of the bleaching increases the amount of damage (molecules lost) but does not change it qualitatively, because the 10 sec time between the bleaching cycles is longer than the time that any change in carrier concentration or temperature persists (*cf.* detailed calculation in SI.6 ESI,† that shows $\Delta T <$ 1 K during the illumination). Fig. 3b-MA shows SEM images of the surface of the MA crystal. Two modes were used: the SE2 detector detects secondary electrons from the (near)surface, which makes it sensitive to surface morphology. The higher surface sensitivity of the In-Lens electron detector makes its signal also sensitive to the electrical potential of the surface, and, thus, reflect the work function.[50,51] Clearly the surface, where the material was bleached (with $\sim$870 μW laser power), is strongly affected by the treatment.

The MA sample formed structures inside the bleached area. As noted above, some signs of the presumed liquid CH_3NH_2-rich phase are also detected by SEM outside the bleached zone (Fig. 3b-MA). However, because SEM is performed in vacuum, the phase that we proposed above as being the cause of the nanoparticles that were observed in the AFM images (Fig. 3a) and of the halo in Fig. 2b-MA-Surface-High LP, evaporates. The InLens image shows an increased signal relative to the background, indicating, as reported earlier,[15,50,51] a decrease in work function. This can be explained by the formation of electron-rich Pb^0 (work function of 4.0 eV,[52] compared to 4.7 to 5.1 eV for the HaP single crystals) over electron-poorer $PbBr_2$ (work function[53] of 6.0 eV). The FA sample (Fig. 3b-FA), even if less stable for a single, defect-inducing bleaching cycle, seems to be more resistant to multiple cycles of bleaching/laser ablation, as seen from the SE2-morphology image. The Cs sample appears to be as affected by the strong laser pulses as the MA one, with an evident change in morphology. Noticeably, for the Cs sample the In-Lens image shows a very strong increase of the signal in the bleached area, indicating a more substantial decrease of the work function than for the MA and FA samples. At the same time, the area around the bleach shows a decrease of signal, corresponding to a work function increase.

3.3 EDS, XPS

To explain the above observations, we examined the surface through EDS and XPS, searching for variation in composition that can explain the above-mentioned observations. EDS analysis shows that photobleaching of the MA sample increases the Pb : Br ratio in the bleached area by a factor of 1.4 compared to the bulk. The signal from a pure $PbBr_2$ crystal would increase

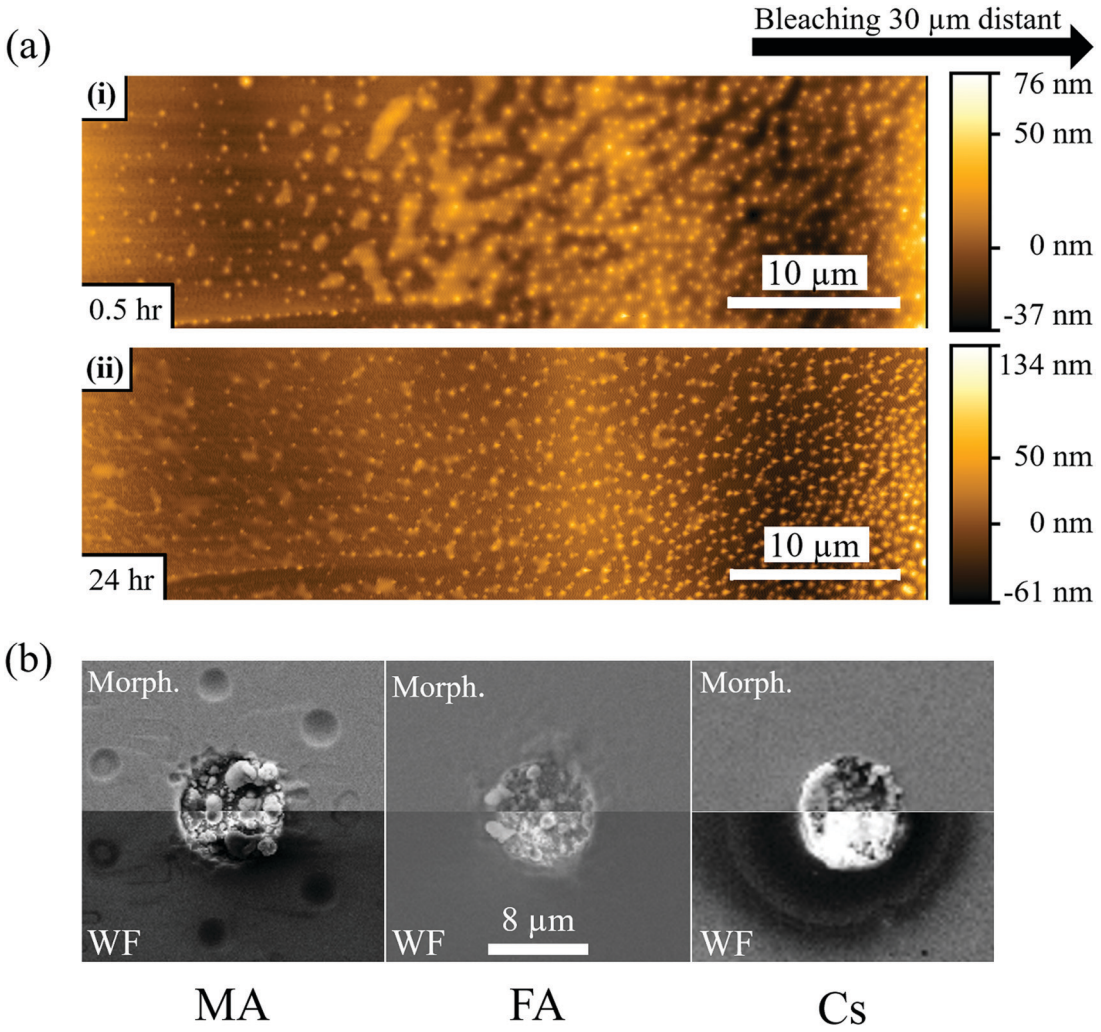

Fig. 3 (a) AFM images of $MAPbBr_3$ single crystal surface 30 min (i) and 24 hours (ii) after 100 cycles of 1P bleaching with a laser power of 880 μW (LP). The AFM image is taken 20–30 μm from the bleached area (see Fig. S6, ESI†), because the AFM tip could not make contact closer to the damaged area. The images show nanoparticles formed on the crystal surface and a semi-liquid phase between the particles that evaporates with time (compare top and bottom AFM images). (b) SEM images of $MAPbBr_3$, $FAPbBr_3$ and $CsPbBr_3$ single crystals after 100 cycles of 1P bleaching with LP. The images were taken with the SE2 detector to show the morphology and with the InLens detector to map variations in work function (whiter for lower, darker for higher work function). The images are mirrored to facilitate comparison between them. For (a) and (b) 100 bleaching cycles were used to increase the amount of damage performed quantitatively. Qualitatively, though, there is no difference as the time delay between each cycle of 10 seconds is longer than any temperature or carrier concentration decay timescale. As is calculated in detail in the ESI† (SI.6), the temperature rise will be less than 1 K.

the Pb : Br signal ratio by a 1.5 factor. At first glance, one could conclude that $PbBr_2$ is formed. However, it has to be taken into account that the EDS signal is collected down to a depth of ~0.5 μm and that the real Pb : Br ratio on the surface is likely much higher. This supports the hint of Pb^0 formation as concluded in the preceding paragraph. On the other hand, no difference in composition, within the sensitivity of EDS, is found between the background and the halo-area around the bleached area. EDS analysis of FA samples, on the other hand, showed only a factor of 1.15 increase in Pb : Br ratio. This is also consistent with Pb^0 formation, although this does not exclude possible $PbBr_2$ formation. Cs samples show no change in the Cs : Pb : Br ratio but a Pb : O ratio of 1.4 : 1 is found, indicating additional oxygen (see SI.13, ESI† – no O is found in the background by EDS).

The XPS analysis (see SI.14, ESI† for Experimental details) of a Cs sample, treated in the same way over a much larger (few mm^2) area, did not show the presence of any Pb oxide, as the Pb spectrum did not differ from that of a non-treated one. XPS revealed, instead, a ~15% increase of the Cs:Pb ratio on the surface. Since any sample is contaminated by oxygen and carbon and XPS cannot differentiate between traces of O coming from perovskite oxidation or from contamination, it is not possible to exploit it to determine O surface concentration. Nevertheless, as the depth analyzed by XPS is 1–2 orders of magnitude smaller than the EDS one, the two results are not contradictory. From the comparison of XPS and EDS, we conclude that Cs enrichment is limited to the surface region. The presence of oxygen is probably an indication of the formation of either lead or cesium oxides or,

lead bromates. The formation of cesium oxides can explain the InLens-work function image of Fig. 3b-Cs, because Cs oxides are known low work-function ($\sim$1 eV) materials.[39,54] We note that neither lead oxide nor lead bromate are stable in acid environment. $MAPbBr_3$ and $FAPbBr_3$ are reactive towards oxides due to the acidity of the A^+ cation and would transform to $PbBr_2$. $PbBr_2$ could then eventually transform to Pb^0 under illumination,[27,28] a photoreaction known also for PbI_2.[55] The possible formation of lead oxides or bromates would deplete the lead content of the original perovskite, leaving a Cs-rich volume that, as reported previously,[36] has a stronger and blue-shifted photoluminescence.

3.4 Support from TGA-MS

Using Mass Spectroscopy (MS – see SI.6, ESI†) we analyzed the decomposition products that are released from $MAPbBr_3$, $FAPbBr_3$ and mixed FA-$CsPbBr_3$ single crystals between 320 °C and 360 °C (during ThermoGravimetric Analysis, TGA). We could detect HBr and CH_3Br from the decomposition of $MAPbBr_3$, implying formation of both CH_3NH_2 and NH_3 (not MS-detectable in our TG-MS because of their low molecular weight). $FAPbBr_3$ decomposed to HBr and triazine. No Br_2 formation was detected from any of these crystals. Therefore, we conclude that their thermal material degradation stops at $PbBr_2$. However, $PbBr_2$ is known to photolyze readily, which means that photobleaching will lead to Pb^0 and Br_2 formation. Unfortunately, illumination of the sample was not possible in those MS systems, that were suitable for our samples and available to us.

4 Chemistry of self-healing in the bulk

In Section 2 of this article, we reported that the A cation strongly modifies both degradation and recovery of the three $APbBr_3$ perovskites. This effect, at least in the bulk, should be explainable on the base of chemical instability of the species formed after photobleaching. One would indeed expect more stable species to heal slower than more unstable ones.

Experimental identification of the chemical origin of such differences in the bulk is not possible given the low amount of defects that the bleaching produces (the material can be considered the same on a macroscopic level). No optical method (the bulk is not accessible otherwise) can indeed identify defects in traces (the effects on the PL intensity that we noticed are most probably produced by under ppb defect density). Because of the difficulty to use experimental methods to get insight into the defect chemistry and physics, we turned to state-of-the-art density functional theory (DFT) to assess the plausibility of pertinent chemical scenarios and to help understand the observed phenomena. Specifically, we focus on deformations caused in the minimum energy structure of the pristine material by introducing a defect, as well as on the degree of charge localization around the defect. For computational details, see SI.9 (ESI†).

4.1 DFT of bromide interstitials: general considerations

The A cation is known to have a minimal direct effect on the HaP electronic structure.[43,44] However, it does influence the structure of the perovskite by changing the cell size and the symmetry, thereby indirectly affecting the defect chemistry of the material. Depending on the A cation, a similar defect can cause varying levels of distortion to the crystal, which can determine whether the defect will have long-term (meta)stability. The more distorted the structure, the less likely it is that the defect will persist, barring kinetic stabilization.

A growing consensus points to halogen related defects, most notably interstitials, as possible traps and/or charge recombination centers in HaPs.[56–59] For this reason, we focus our efforts on interstitial bromide defects in all three systems. In the point defect model, an interstitial defect can have different charge states, depending on the energy of its charge transition level relative to the Fermi level of the material. Specifically, a Br interstitial defect can be either positively charged (Br_i^+), neutral (Br_i^0), or negatively charged (Br_i^-). Experimentally, HaPs are commonly found to be slightly p-type,[60,61] *i.e.*, with a Fermi level that is closer to the level of the valence band maximum (VBM) than the conduction band minimum (CBM) and lower than the defect level. This suggests that a positively charged defect is the most probable one.

4.2 Br_i^+: geometry in the three $APbBr_3$ HaPs

Using DFT, we calculated the minimum energy structure of a Br interstitial in each of its possible charge states, in all three systems. The Br_i^+ structures are presented in Fig. 4a–c. For completeness, all other calculated minimum energy structures are reported in SI.8 (ESI†). In all three systems, the Br_i^+ defect produced a similar structure: the Br_i^+ relaxed to a position between two neighboring lattice Br anions, connecting two octahedral cages to create a rigid, linear Br_3^- structure with Br–Br distances of 0.255–0.259 nm. Br_3^- anions are known constituents of solids, *e.g.* $CsBr_3$,[62] and other organic cation equivalents[63] or ionic liquids[64] (*e.g.*, $MaBr_3$ and $FABr_3$).[15] Linear polyhalide anion species generated by interstitial Br have also been observed experimentally in some crystal structures, *e.g.* KCl,[65,66] KBr,[65,66] RbBr,[67] and CsBr.[68]

We find that the room temperature (RT) orthorhombic $CsPbBr_3$ structure remains almost undistorted around the defect, whereas the RT cubic $MAPbBr_3$ and $FAPbBr_3$ structures are strongly perturbed. In particular, in $MAPbBr_3$ and $FAPbBr_3$, one of the bromine atoms has to shift strongly off the axis formed by the two Pb ions to which it is bound, in order to bind to the Br interstitial ion (see the displacement (Δ) of the topmost Br atoms, marked in purple in Fig. 4b and c (red arrows)). As a consequence, the interstitial Br atom and the second structural Br atom are pushed downwards and away from the latter's equilibrium position. While for $MAPbBr_3$ the MA^+ orientations remain relatively unchanged, in the case of FA^+ the presence of a Br interstitial defect causes a strong modification of the equilibrium positions of the nearby FA^+ ions (see ions indicated by light blue arrows, Fig. 4c). In addition, reaching converged

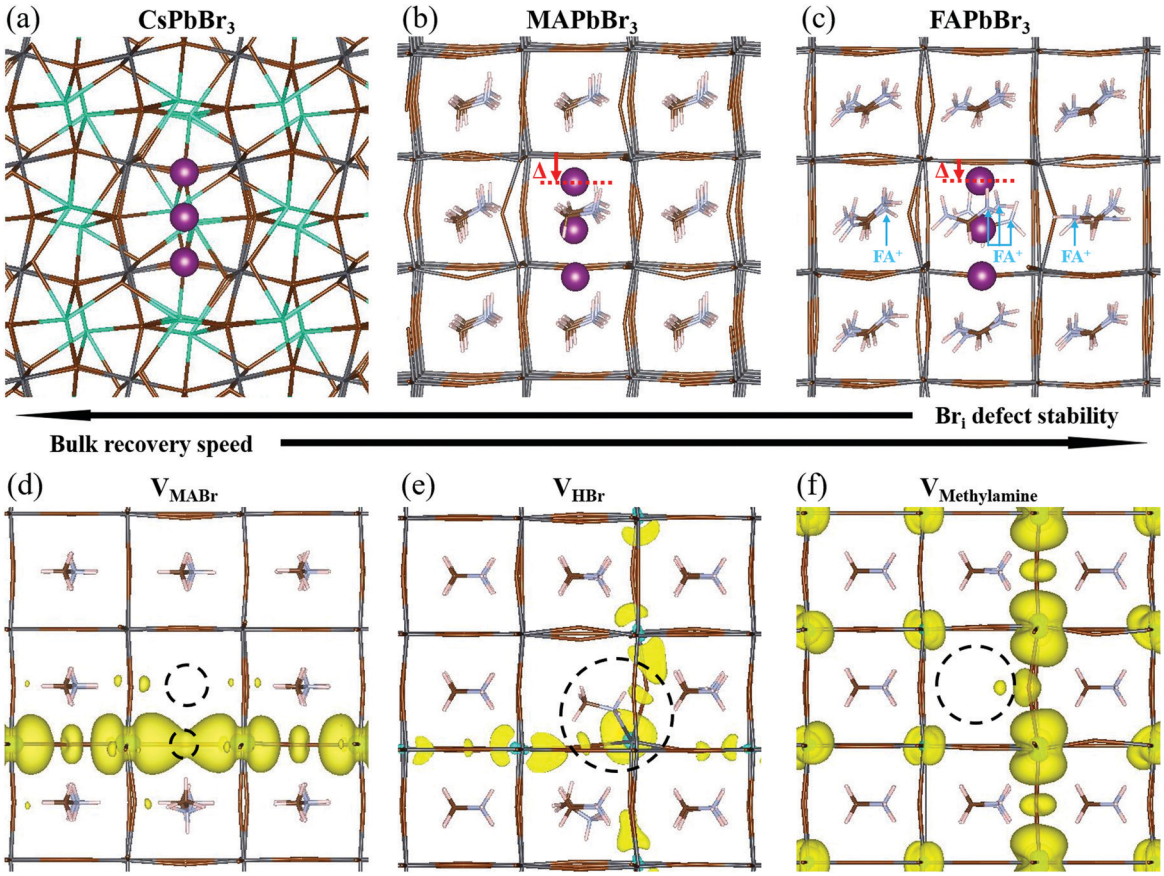

Fig. 4 Minimum energy structures of (a) orthorhombic $CsPbBr_3$, (b) cubic $MAPbBr_3$, and (c) cubic $FAPbBr_3$, containing a Br_i^+ defect, as well as minimum energy structures of $MAPbBr_3$ containing (d) V_{MABr}, (e) V_{HBr}, and (f) V_{MeNH2}. Br_i^+ defects are marked in purple and vacancies are marked by dashed circles. Cs atoms are marked in green, Pb atoms in dark grey, and Br atoms in brown. The red arrow indicates the displacement of the Br atoms from the Br–Pb–Br axis. The light blue arrows indicate the FA^+ ions most affected by the defect. Yellow contours in (d)–(f) represent the partial charge density associated with the defect eigenvalue.

minimum energy geometries for the Br interstitial in $FAPbBr_3$ is much more difficult than in $MAPbBr_3$ and $CsPbBr_3$. This, coupled to the large structural distortions in the $FAPbBr_3$ system, indirectly indicates the improbability of a stable Br interstitial in that material. We can speculate that FA^+, by way of its natural vibration, will "push" Br_i^+ out towards the next nearby equilibrium Br position (in the octahedral cage), with consequent displacement of the already-present Br ion that becomes an interstitial defect in the next unit cell. This process will repeat until the interstitial recombines with a vacancy or is otherwise annihilated.

4.3 Br_i^+: relation between geometry and stability

Our DFT calculations suggest that the self-healing in the bulk of the $APbBr_3$ could be inversely related to the amount and localization of the deformation introduced by the Br interstitial.[69] The stability of a Br interstitial defect is lowest for $FAPbBr_3$, whereas in $CsPbBr_3$ the defect can exhibit long term metastability. It is important to note that it has recently become clear that the perovskite structure is not static, but rather is subject to large, anharmonic, polar fluctuations.[70–72] Moreover, these fluctuations may affect the defect energy landscape.[73] Clearly, the static, relaxed structure can only represent an average picture. Because the static FA^+-containing structure is already greatly distorted even in the absence of dynamic effects, much more so than the Cs^+-containing one, it is reasonable to assume that these differences carry over to the dynamic, room temperature systems.

4.4 The role of methylamine

In Section 2 we noted that $MAPbBr_3$ exhibits increased PL brightness upon photo-bleaching in the bulk, whereas the two other bromide perovskites do not. This necessitates further examination of the consequences of an MA-related defect, also in the view that all reported cases of light soaking in HaPs contain MA in the composition (see ref. 74 for a recent review on the subject). Free methylamine possibly forms in the bulk after dissociation of the methylammonium to methylamine and HBr. We therefore look into three neutral defect complexes involving methylamine and bromine: (1) an MABr vacancy, V_{MABr}; (2) an HBr vacancy, V_{HBr}; (3) a methylamine vacancy, V_{MeNH2}.

In Fig. 4d, we show the structure and charge density associated with V_{MABr}. In this case, the charge density is localized along the

Pb–V_{Br}–Pb axis. For the V_{HBr} (Fig. 4e), the charge density spreads two dimensionally, while for the V_{MeNH_2} (Fig. 4f) the defect induces a smaller effect with an almost unchanged geometry and a rather delocalized charge density in all three dimensions. This indicates a negligible effect on the electronic structure and a very low likelihood of trap formation. We stress that for the V_{HBr}, we report a direct bond between the lone pair of the N atom of methylamine and the nearest Pb atom. When removing HBr (as well as MABr), two Pb–Br bonds are broken, creating a defect level in the gap. The additional electron density, due to the lone pair on the N atom in CH_3NH_2, partially screens the defect, making V_{HBr} less harmful than V_{MABr}. However, V_{HBr} and V_{MeNH_2} are not the thermodynamically favored structures. According to our calculations, the reaction:

$$V_{HBr} + V_{MeNH_2} \leftrightarrow V_{MABr}$$

results in a 1.9 eV reduction in energy, indicating that the methylamine is likely to migrate back to recombine with the HBr "left behind", thereby restoring the MABr vacancy. This explains why the more luminescent state, formed under photo-bleaching and comprised of V_{HBr} and V_{MeNH_2}, reverts to the original state, V_{MABr}, with time. Notably, such kinetics should strongly depend on the migration speed of protons, which should also depend on the H_2O concentration in the perovskite structure.[75,76]

5 General discussion: pulling it all together

The presented data show the differences in degradation and self-healing between surface and bulk and between $MAPbBr_3$, $FAPbBr_3$, and $CsPbBr_3$. These variations can be crucial in determining the stability of HaP materials and HaP-based devices.

To understand the atomistic processes that lead to the reported results we consider:

- how the A cation influences self-healing on both the surface and in the bulk of HaPs;
- how the A cation influences the defect density in the HaPs;
- how "proper" encapsulation has to take into account all processes we have identified, rather than being limited to preventing H_2O and O_2 penetration in the HaP-based device.

5.1 Surface and bulk stability: the role of the A cation

In Fig. 5 and in Table 1 we summarize all the information on $APbBr_3$ perovskites after photo-bleaching, provided by the current study. Closed circles represent degradation followed by self-healing processes. Red circles describe Br_i-related ones and green circles describe methylamine-related processes. Thicker lines correspond to faster processes. Arrows pointing vertically represent material exchange with the environment. Bulk and surface processes are separated by the dotted line, showing that self-healing dominates in the bulk and material loss dominates at the surface.

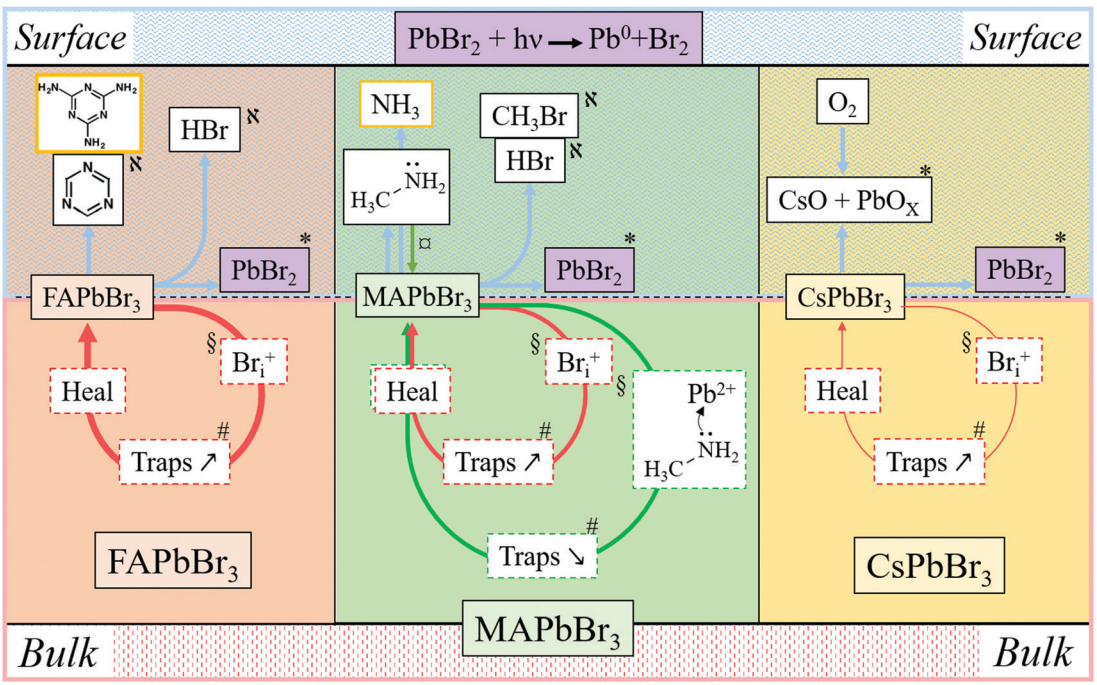

Fig. 5 Scheme of the chemical processes involved in the degradation and healing of $APbBr_3$ perovskites on the surface and in the bulk. Information from the literature is contained in orange rectangles. Surface phenomena are reported in the upper row and bulk ones in the row below, under the dashed line. The thickness of the arrows (for the degradation on the surface and the self-healing in the bulk) corresponds qualitatively to the speed of the corresponding process. The symbols indicate observables, analyzed in the main text, and consistent with the indicated processes: § DFT; # 2P PL Lifetime and intensity; ¤ 1P PL Intensity and AFM; * InLens SEM, EDS and work function increase; ℵ TGA-MS. On $MAPbBr_3$ and $FAPbBr_3$ PbO will not be because it reacts with $CH_3NH_3^+$, $H_2NCHNH_2^+$ to give CH_3NH_2, $HNCHNH_2$ and H_2O.

Table 1 Summary of the damage and self-healing and additional phenomena reported in this work for the $APbBr_3$ perovskites

Cation	Location	Damage	Healing	Phenomenon	Supported by
MA	Surface	Threshold	Minimal	Halo – MA condensation, Pb/Br increase	AFM – SEM, EDS
	Bulk	Progressive	Fast	Increase/decrease in PL	DFT
FA	Surface	Threshold	Partial	Pb/Br increase	EDS
	Bulk	Progressive	Very fast	Decrease in PL	DFT
Cs	Surface	Threshold	Semi-complete	O-containing product(s), Cs/Pb increase	EDS, XPS
	Bulk	Progressive	Slow	Decrease in PL	DFT

Each of the indicated processes is consistent by results from experiments and computations, as indicated by symbols.

5.1.1 FA HaP. Analyzing the results for the FA HaP (left column in Fig. 5), we see how FA heals completely and rapidly (thick red curved line) in the bulk, while showing mostly irreversible damage at the surface. DFT results (Section 4.2) show how, due to steric effects, FA^+ ions around the Br_i^+ are displaced from their equilibrium position in the defect-free structure. It is reasonable to think that the found configuration is then energetically unfavorable. The system will try to revert to its defect-free form, explaining the complete self-healing in the bulk. At the same time, surface results show that, once damaged, FA becomes more stable than MA. Unlike methylammonium, formamidinium does not decompose to an amine – acid couple, but decomposes to higher boiling point organic (aromatic) molecules *i.e.* triazine (this work) or sym-triazine:[77,78]

$$FAPbBr_3 + h\nu \leftrightarrow FABr + PbBr_2 \quad (a)$$

$$FABr \leftrightarrow \text{(sym)-triazine} + \text{other decom. products} \quad (b)$$

5.1.2 MA HaP. Examining the effects of the MA cation on the 2P bulk processes (center column in Fig. 5), we observed two opposing transient phenomena (*cf.* Fig. 1b): one increases the PL at medium LP (indicated by the green arrow), and another one decreases the PL, as in the FA and Cs samples. The first effect is ascribed to passivation by methylamine (Section 4.3), generated by decomposition of methylammonium. The second effect is ascribed to the chemistry of the Br_3^- species in the form of the interstitial Br defect (Br_i^+), suggested by DFT (Sections 4.1 and 4.2).

Considering now the surface process, the MA perovskite decomposition proceeds, as indicated by our MS results and the AFM results, as follows:[12,13]

$$MAPbBr_3 + h\nu \leftrightarrow MABr + PbBr_2 \quad (c)$$

$$MABr \leftrightarrow CH_3NH_2\uparrow + HBr\uparrow \quad (d1)$$

$$MABr \leftrightarrow CH_3Br + NH_3\uparrow \quad (d2)$$

Above, we argued that CH_3NH_2 from reaction (d1) re-condenses on the crystal surface (Sections 3.1 and 3.2), eventually re-evaporating over long times. It was shown[12] that CH_3NH_2 can be formed from $MAPbBr_3$ (films) under 1 sun illumination consistently to our detection of HBr. After degradation, it is probable that if the system is not in vacuum, at least some CH_3NH_2 is reabsorbed at the surface, yielding its known beneficial effect on the material.[45,79] This phenomenon can explain at least part of the reported improvement of the $MAPbBr_3$ properties after a short illumination period (light-soaking), reported in the literature.[80,81]

In the bulk material, the products of reaction (d1) can be absorbed by the crystal without forming a gas: methylamine, as discussed above (Section 4.3), can penetrate the crystal structure, HBr can dissociate into H^+, which can penetrate into the structure due to its small size, while Br^- can be accepted as part of an interstitial defect. CH_3Br, however, is a hydrophobic molecule that does not readily react either with the perovskite or with NH_3. Its formation would build up extremely high pressure inside the crystal. This reasoning rationalizes that reaction (d2) is inhibited in the bulk by the law of mass action. However, in contact with an organic HTL, ETL or encapsulating polymer, CH_3Br will be readily absorbed, pushing the reaction to the right and leading to irreversible decomposition, even if the device is encapsulated.

5.1.3 Comparing $MAPbBr_3$ and $FAPbBr_3$. Reaction (c), involving $MAPbBr_3$, needs more energy to be pushed to the right by light (damage threshold 60% of LP, full line Fig. 1a) than reaction (a) involving $FAPbBr_3$ (threshold 45% LP, full line Fig. 1c). Further MABr decomposition (d1) and (d2) needs less energy than that of FABr (b) (*cf.* Fig. 1a and c, full lines). After the initial decomposition (b), the (sym)-triazine that formed does not leave the bleaching site as easily as CH_3NH_2, HBr, CH_3Br and NH_3, the MABr decomposition products (d1) and (d2), as it is has a higher boiling point and lower vapor pressure than those molecules. Therefore, (sym)-triazine pushes the equilibrium of the decomposition reaction to the left. The result is that reaction (b) is less likely to happen, more products of equation (a) remain and some self-healing happens at the surface to a greater extent than what is the case for its MA equivalent.

5.1.4 Cs HaP. The situation is different for the $CsPbBr_3$ sample (right column in Fig. 5). From the DFT computations (Sections 4.1 and 4.2) we learn that in the bulk the formation of a Br_3^- defect is not energetically expensive, as it does not significantly impact the crystal structure. This result explains, at least partially, why self-healing of the Cs HaP in the bulk is slow and the material's recovery is slower than that of its analogs with organic A cation. At the surface, $CsPbBr_3$ has a greater ability to rearrange its structure as movements of atoms on the surface are less sterically hindered. Because of this, the migration of the products of decomposition (excluding the oxides) is easier than in the bulk once the decomposition happens. Notably, at the surface (Fig. 1e) the minimum light intensity at which the Cs sample is damaged is lower than for the MA one. Thus, intrinsically, $CsPbBr_3$ is less stable than the MA analogue. The LP threshold

of damage (*cf.* Fig. 1a, c and e full lines) can be viewed as a proxy for the activation energy of the decomposition reaction. We can then conclude that the activation energy for Cs decomposition on the surface is less than that for MA decomposition and similar to that for FA decomposition. Still, its stability in normal use can be attributed to its better (less problematic) self-healing properties at the surface (*cf.* dashed lines in Fig. 1e with dashed lines in Fig. 1a and c).

Interestingly, only for $CsPbBr_3$ do we find formation of a non-healable form with more intense PL inside the bleached area in the 1P-surface experiment at high LP (Fig. 1e, 2a and 3b). This result is explained by the reaction of $CsPbBr_3$ with oxygen, as shown by EDS, which indicates formation of an O-containing product. XPS shows formation of a Cs-rich surface (Section 3). This decomposition pathway creates a PL increase only if the surface of the material is exposed to O_2 (which is the case under our experimental conditions) and to light. Still, this strong bleaching-induced modification of the surface does not improve the PL lifetime, despite increasing its intensity (Fig. 2b-Cs-High LP).

Overall, surface decomposition of $CsPbBr_3$, even if starting at lower energies than in the MA case, is less impactful than for FA and MA, probably because only a small amount of volatiles is actually created and most of the material can re-form (and, likely, quicker than in the bulk, as steric constraints are relaxed).

5.1.5 $Br_{2(g)}$ formation. The SEM-inLens and EDS results on $MAPbBr_3$ and $FAPbBr_3$ perovskites gave strong hints for the formation of metallic Pb^0 on the surface. Pb^0 formation implies Br_2 loss from the material. Unfortunately, we could not perform MS during bleaching for technical reasons/instrumental limitations. Br_2 formation upon $MAPbBr_3$ and $FAPbBr_3$ illumination is expected from the known photo-decomposition (photolysis) of $PbBr_2$ to Pb^0 and Br_2,[27,28] similar to PbI_2 decomposition,[55] and from analogy with $FAPbI_3$ or $MAPbI_3$ perovskites, which were shown to release I_2 upon illumination.[12,82] Also, Pb^0 and consequent Br_2 loss was identified by other groups after e-beam[83] or X-ray.[84] It is reasonable to think that, with time, Pb^0 will react with the slightly acidic MA^+/FA^+ cations forming H_2, methylamine/formamidine and $PbBr_2$. Pb^0 could then have a limited timespan on the surface of the perovskite if no new light-damage is induced.

5.1.6 Comprehensive view. By integrating the data and their evaluations for the three HaPs that we studied, we can consider the case of mixed A cation perovskites $MA_xFA_yCs_{1-x-y}PbBr_3$: Cs helps to stabilize the surface of the material, as $CsPbBr_3$ cannot decompose further under normal cell working conditions and in the absence of reactive ambient (*e.g.* H_2O). Under optimal working conditions, the Cs, MA and FA HaPs should, after exposure to sunlight, start to achieve a state where most of the surface is Cs-rich, some methylamine is released and able to migrate into the bulk to heal defects, and the formamidinium grants the long-term stability thanks to its superior bulk self-healing properties. We can speculate that at steady state (of illumination), the A cation distribution does not remain uniform and evolves towards a Cs-enriched stabilized surface and an FA-enriched self-healing-promoting bulk. In the future, this model can be tested by, *e.g.*, ToF-SIMS experiments of films or crystals, exposed to light for long times. Such experiments are planned.

Summarizing, each A cation influences the chemistry and self-healing of the perovskite differently. When the A cations are mixed, each of them can synergistically contribute to the overall stability and performance of the material. This synergism is in addition to configurational entropy gains of the system, due to lack of order in A cation distribution.

5.2 Importance of self-healing for bulk defect density

The FA^+ cation plays here the role of keeping the defect density low. As the defect density is crucial for HaP-based solar cells, we can understand why FA^+ is the most abundant cation in $MA_xFA_yCs_{1-x-y}PbBr_3$ based solar cells.

At equilibrium, a material's self-healing kinetics are connected to its defect density.[85] For every defect, we consider that the defect density is determined by the equilibrium between formation and destruction (by healing) of the defect:

$$APbBr_3 \underset{k_{\text{self-healing}}}{\overset{k_{\text{formation}}}{\rightleftharpoons}} \text{defect} \qquad \text{(e)}$$

For any defect, the equilibrium defect density [defect] is:

$$(f)[\text{defect}] = K_{\text{eq}} \cdot [\text{HaP}] = \frac{k_{\text{formation}}}{k_{\text{self-healing}}} \cdot [\text{HaP}]$$

where [HaP] is the concentration of the perovskite, which is effectively constant for any relevant [defect]. From this we deduce that the [defect] is inversely proportional to the self-healing kinetic constant. We can then expect $FAPbBr_3$ to have the lowest defect density, as its self-healing kinetics are fastest. The effect is particularly relevant during solar illumination. In this case, loss of efficiency is commonly attributed to the formation of defects that are continuously created by illumination.[18,86] The self-healing process continuously repairs (*i.e.* eliminates) the defects, dictating a steady-state defect density that normally will be higher than the equilibrium one. The faster the recovery kinetics, the closer the steady-state defect density is to the equilibrium one as dictated by thermodynamics. Therefore, self-healing protects the material from damage, enhancing its chemical stability and decreasing the steady state density of performance-damaging defects.

5.3 Relation between self-healing and encapsulation

For self-healing to take place, any material loss has to be avoided to minimize the occurrence of reactions like (a) and (c). For this reason, it is now necessary to redefine what ''proper'' encapsulation is in the case of HaPs. There are many reports on how classical encapsulation significantly improves the stability of halide perovskite solar cells. This is not surprising, as the most obvious effect of encapsulation is protecting the material(s) against chemical attacks (*i.e.* H_2O, O_2) from the ambient. However, this is not all that encapsulation should do.

5.3.1 The new role of encapsulation. It is well-known that electronic devices need to be protected against the environment for especially reactions with O_2 and H_2O. This holds even more so for photovoltaic cells, nearly all of which are employed

outside and meant to last for decades. HaP-based PV is no exception and this was realized esp. for iodide-based perovskites (*cf.*, for example, ref. 87), where also the importance of containing decomposition products was stressed (*cf.*, *e.g.*, ref. 88).

The critical new insight from our study is that besides protecting from external chemical attack, and containing decomposition products, which will by the mass-action law, increase the probability of re-composition, this will allow self-healing to occur also at and near the surface. This insight shows that proper encapsulation can act beyond protection and containment by conveying also to the surface of the HaP (and its interfaces in devices) dynamic stabilization.

The self-healing that we demonstrated to occur in bulk perovskites requires any decomposition product to be readily available, to enable reversal of the decomposition reaction. This condition is clearly not fulfilled at a surface that is open to the ambient, with the consequence that self-healing will be limited. In most reported studies, the ''escape'' ways for decomposition products in HaP-based solar cells are not controlled. For example, an iodine (or bromine) molecule forming at the surface of a solar cell may well find its way between grain boundaries or through the larger than molecular spaces between the perovskite layer and the HTL (or in the porous, if not completely filled ETL as in case of mesoporous TiO_2). Eventually the molecule can get away from the HaP surface and, for example, accumulate in open spaces. In such case, even if the product of the decomposition has not reacted with the ETL or HTL, but ends up spatially far from the decomposition site, it may not be available for self-healing.

5.3.2 Relevance for organic HTL. The problem of material loss in other layers of the solar cell is particularly important for HTL materials. Most HTLs used today are not resistant to acids (HBr, HI), bases (methylamine, formamidine), organic molecules (CH_3I, CH_3Br), the types of organic solvents used during HaP preparation, and/or halogens (Br_2, I_2), each of which may be formed/released by halide perovskite degradation. Most organic HTL materials, such as spiro-OMeTAD,[89] poly-thiophenes[90] (P3HT, PTB7, *etc.*) and poly-triarylamine PTAA, will eventually absorb or react with some or all decomposition products. With few exceptions, such as PCBM[91] (phenyl-C61-butyric acid methyl ester), ETLs are inorganic oxides, which will mostly be more stable than organic ones.

The above issues point to one reason why hybrid 3D–2D perovskites can have enhanced stability and optoelectronic properties. The organic layers of these perovskites can prevent escape of any 3D decomposition products. Such an effect would be in addition to passivation of defects on the surfaces of the 3D perovskites, by adding the 2D layers as well as increased hydrophobicity to keep water away.

6 Conclusions

We compared and contrasted experimentally bulk and surface damage of $APbBr_3$ halide perovskites and evaluated the results using thermodynamic, kinetic, chemical, and physical considerations. We demonstrated how the intrinsic stability of the perovskites, linked to thermodynamics, is significantly greater than their kinetic stability, thanks to self-healing. We performed PL, FLIM, AFM, EDS and XPS measurements, and DFT simulations to analyze and explain the differences in the damage that can be inflicted by a strong laser beam, and the self-healing processes for the three different A cation perovskites.

FA provides superior healing properties in the bulk of the material and reduces the bulk defect density because of the instability of the Br_i^+ defect (in a Br_3 complex) in its structure, differently from what happens in MA and Cs. When photo-excited in the bulk, MA decomposes to methylamine and HBr (eqn (c) and (d1)). Methylamine can migrate and passivate defects while H^+ remains at the site of the MA^+ ion without serious effect on the local electronic properties. This causes an increase of PL (and probably in photo-conversion) efficiency, increasing solar cell performance. Finally, Cs^+ helps to stabilize the surface of the material.

In terms of fundamental understanding, our results lead us to hypothesize about the question of why HaPs have such good optoelectronic, and particularly PV properties, expressed by (a) relatively long charge carrier lifetimes and diffusions lengths. These qualities can be traced to (b) low densities of electronically and optically active defects, *i.e.*, those that affect measurable properties. As (a) will be qualitatively inversely proportional to (b), if the defects are subject to self-healing, their density will be small. Taken to the extreme, self-healing becomes the fundamental cause for the excellent optoelectronic properties of the HaPs, because all derive from the self-healing. Even if self-healing is not the sole cause, it likely is a major reason for the HaPs' excellent properties.

We stress how from our results we can infer that fulfilling the conditions for self-healing is necessary for long-lasting stability of devices made with HaP materials. In particular, apart from perfect encapsulation, the ETL and HTL have to be chemically unreactive towards the decomposition products of the perovskites in order to create ''bulk-like'' conditions for the HaP part of the interfaces. In the most stable devices that were reported, such an effect was likely an unintended consequence, in-depth analysis of which can help deciding on device architectures for commercialization.

Author contributions

D. R. Ceratti originated the idea of using a 2P/1P microscopy-based approach to assess perovskite stability, and using FRAP as reporting method; he synthetized the single crystals used in this study, collected and analyzed the data. G. Hodes* and D. Cahen* defined the problem and participated with DRC in analyzing and interpreting the data. DRC wrote the initial draft and with DC, GH and LK finalized the paper. A. V. Cohen* and L. Kronik* performed the DFT simulations and wrote that part of the text. R. Tenne,* M. Elbaum* and V. Kalchenko made possible the 1P and 2P microscopy experiments and helped DRC to acquire and

analyze those data. Y. Rakita helped synthesize $CsPbBr_3$ crystals and performed with DRC the SEM and EDS measurements. T. Bendikov performed and analyzed the XPS measurements. L. Snarski helped unravel the chemistry of methylamine. L. Cremonesi* and M. A. C. Potenza* performed the calculations on the focusing and aberration effects for the 1P and 2P laser beam experiments at the surface and inside the crystals. They participated with DRC in calculating the effective energy deposited inside the material and wrote the ESI† one these calculations. I. Rosenhek-Goldian acquired the AFM images with DRC. I. Kaplan-Ashiri performed the simulations of EDS penetration and emission profiles and wrote the relevant text. N. P. Jasti, R. Cohen and M. Weitman performed and analyzed the TGA measurements. The authors here marked with a * reviewed the final text before submission, helping to clarify and simplify the text.

Conflicts of interest

There are no conflicts to declare.

Acknowledgements

We thank Dan Oron (Weizmann Inst.) for many fruitful and stimulating discussions. D. R. C. thanks the Weizmann Institute's SAERI, Sustainability And Energy Research Initiative, for a 2017–2020 PD fellowship in the first 2 years of which this work was done; D. R. C. and D. C. thank the Minerva Center for Self Repairing Systems for Energy and Sustainability for partial funding; D. C. thanks the Ullmann family foundation for partial 2017–2018 funding, when the research was done. Y. R. acknowledges a 2018 Perlman research grant for student-initiated research in chemistry for partial support. A. V. C. and L. K. acknowledge support by the Minerva Foundation. L. K. holds the Aryeh and Mintzi Katzman Professorial Chair. D. C. also thanks the Yotam project of the WIS' SAERI, for partial support. D. R. C. held a SAERI PD fellowship. N. P. Jasti acknowledges funding from the European Union's Horizon 2020 MSCA Innovative Training Network under grant agreement no. 764787 (MAESTRO). D. R. C. thanks Ilario Gelmetti, Stefania Cacovich and Alexandre Py for fruitful discussions and clarity check of the text.

Notes and references

1 M. A. Green, Y. Hishikawa, E. D. Dunlop, D. H. Levi, J. Hohl-Ebinger, M. Yoshita and A. W. Y. Ho-Baillie, *Prog. Photovolt. Res. Appl.*, 2019, **27**, 3–12.
2 Q. Jiang, Z. Chu, P. Wang, X. Yang, H. Liu, Y. Wang, Z. Yin, J. Wu, X. Zhang and J. You, *Adv. Mater.*, 2017, **29**, 1703852.
3 T. M. Brenner, D. A. Egger, L. Kronik, G. Hodes and D. Cahen, *Nat. Rev. Mater.*, 2016, **1**, 1–16.
4 H. Kim, J. S. Han, J. Choi, S. Y. Kim and H. W. Jang, *Small Methods*, 2018, **2**, 1700310.
5 C. C. Stoumpos and M. G. Kanatzidis, *Adv. Mater.*, 2016, **28**, 5778–5793.
6 L. N. Quan, B. P. Rand, R. H. Friend, S. G. Mhaisalkar, T.-W. Lee and E. H. Sargent, *Chem. Rev.*, 2019, **119**, 7444–7477.
7 Y. He, L. Matei, H. J. Jung, K. M. McCall, M. Chen, C. C. Stoumpos, Z. Liu, J. A. Peters, D. Y. Chung, B. W. Wessels, M. R. Wasielewski, V. P. Dravid, A. Burger and M. G. Kanatzidis, *Nat. Commun.*, 2018, **9**, 1609.
8 S. He, L. Qiu, L. K. Ono and Y. Qi, *Mater. Sci. Eng., R*, 2020, **140**, 100545.
9 B. Chen, P. N. Rudd, S. Yang, Y. Yuan and J. Huang, *Chem. Soc. Rev.*, 2019, **48**, 3842–3867.
10 Y. Lin, Y. Bai, Y. Fang, Z. Chen, S. Yang, X. Zheng, S. Tang, Y. Liu, J. Zhao and J. Huang, *J. Phys. Chem. Lett.*, 2018, **9**, 654–658.
11 X. Zhang, X. Ren, B. Liu, R. Munir, X. Zhu, D. Yang, J. Li, Y. Liu, D.-M. Smilgies, R. Li, Z. Yang, T. Niu, X. Wang, A. Amassian, K. Zhao and S. (Frank) Liu, *Energy Environ. Sci.*, 2017, **10**, 2095–2102.
12 E. J. Juarez-Perez, L. K. Ono, M. Maeda, Y. Jiang, Z. Hawash and Y. Qi, *J. Mater. Chem. A*, 2018, **6**, 9604–9612.
13 A. E. Williams, P. J. Holliman, M. J. Carnie, M. L. Davies, D. A. Worsley and T. M. Watson, *J. Mater. Chem. A*, 2014, **2**, 19338–19346.
14 D. Prochowicz, R. Runjhun, M. M. Tavakoli, P. Yadav, M. Saski, A. Q. Alanazi, D. J. Kubicki, Z. Kaszkur, S. M. Zakeeruddin, J. Lewiński and M. Grätzel, *Chem. Mater.*, 2019, **31**, 1620–1627.
15 D. R. Ceratti, Y. Rakita, L. Cremonesi, R. Tenne, V. Kalchenko, M. Elbaum, D. Oron, M. A. C. Potenza, G. Hodes and D. Cahen, *Adv. Mater.*, 2018, **30**, 1706273.
16 Here we use self-healing to describe the series of chemical processes that undo damage in a material or system, without the involvement of any external factors/effects. We distinguish it from self-repair, which is used also to describe the ability to repair more complex systems, not by net reversal of the mechanisms that led to the damage, but through different actions that can involve other factors/effects, triggered without external intervention, to mend the damage.
17 The system has to be made as closed as possible, *i.e.*, limiting exposure to ambient and especially escape of eventual possible products as much as possible. These layers must not solubilize or react with the products of decompositions of the HaPs, so as to make the HaP thin film bulk-like.
18 W. Nie, J.-C. Blancon, A. J. Neukirch, K. Appavoo, H. Tsai, M. Chhowalla, M. A. Alam, M. Y. Sfeir, C. Katan, J. Even, S. Tretiak, J. J. Crochet, G. Gupta and A. D. Mohite, *Nat. Commun.*, 2016, **7**, 11574.
19 J. Fan, Y. Ma, C. Zhang, C. Liu, W. Li, R. E. I. Schropp and Y. Mai, *Adv. Energy Mater.*, 2018, **8**, 1703421.
20 F. Lang, N. H. Nickel, J. Bundesmann, S. Seidel, A. Denker, S. Albrecht, V. V. Brus, J. Rappich, B. Rech, G. Landi and H. C. Neitzert, *Adv. Mater.*, 2016, **28**, 8726–8731.
21 C. Ran, W. Gao, J. Li, J. Xi, L. Li, J. Dai, Y. Yang, X. Gao, H. Dong, B. Jiao, I. Spanopoulos, C. D. Malliakas, X. Hou, M. G. Kanatzidis and Z. Wu, *Joule*, 2019, **3**, 3072–3087.
22 C. Wang, F. Gu, Z. Zhao, H. Rao, Y. Qiu, Z. Cai, G. Zhan, X. Li, B. Sun, X. Yu, B. Zhao, Z. Liu, Z. Bian and C. Huang, *Adv. Mater.*, 2020, **32**, 1907623.

23 B. Wenger, P. K. Nayak, X. Wen, S. V. Kesava, N. K. Noel and H. J. Snaith, *Nat. Commun.*, 2017, **8**, 590.
24 Q. Dong, Y. Fang, Y. Shao, P. Mulligan, J. Qiu, L. Cao and J. Huang, *Science*, 2015, **347**, 967–970.
25 R. Heiderhoff, T. Haeger, N. Pourdavoud, T. Hu, M. Al-Khafaji, A. Mayer, Y. Chen, H.-C. Scheer and T. Riedl, *J. Phys. Chem. C*, 2017, **121**, 28306–28311.
26 N. Onoda-Yamamuro, T. Matsuo and H. Suga, *J. Phys. Chem. Solids*, 1990, **51**, 1383–1395.
27 J. F. Verwey and J. Schoonman, *Physica*, 1967, **35**, 386–394.
28 J. Schoonman and J. F. Verwey, *Physica*, 1968, **39**, 244–250.
29 M. B. Islam, M. Yanagida, Y. Shirai, Y. Nabetani and K. Miyano, *Sol. Energy Mater. Sol. Cells*, 2019, **195**, 323–329.
30 L. Shi, M. P. Bucknall, T. L. Young, M. Zhang, L. Hu, J. Bing, D. S. Lee, J. Kim, T. Wu, N. Takamure, D. R. McKenzie, S. Huang, M. A. Green and A. W. Y. Ho-Baillie, *Science*, 2020, **6497**, eaba2412.
31 D. Cahen and L. Chernyak, *Adv. Mater.*, 1997, **9**, 861–876.
32 K. T. Arulmozhi and N. Mythili, *AIP Adv.*, 2013, **3**, 122122.
33 M. M. Amini, E. Najafi, A. Dehghani and S. W. Ng, *J. Mol. Struct.*, 2015, **1083**, 221–228.
34 I. A. Kamenskikh, A. Kirm, V. N. Kolobanov, V. V. Mikhailin, P. A. Orekhanov, I. N. Shpinkov, D. A. Spassky, A. N. Vasil'ev, B. I. Zadneprovsky and G. Zimmerer, *IEEE Trans. Nucl. Sci.*, 2001, **48**, 2324–2329.
35 V. Gonzalez, D. Gourier, T. Calligaro, K. Toussaint, G. Wallez and M. Menu, *Anal. Chem.*, 2017, **89**, 2909–2918.
36 Y. Rakita, N. Kedem, S. Gupta, A. Sadhanala, V. Kalchenko, M. L. Böhm, M. Kulbak, R. H. Friend, D. Cahen and G. Hodes, *Cryst. Growth Des.*, 2016, **16**, 5717–5725.
37 C. Sun, Z. Gao, H. Liu, C. Geng, H. Wu, X. Zhang, C. Fan and W. Bi, *Dalton Trans.*, 2018, **47**, 16218–16224.
38 J. C. Hamill, J. Schwartz and Y.-L. Loo, *ACS Energy Lett.*, 2018, **3**, 92–97.
39 F. Zhang, J. C. Hamill, Y.-L. Loo and A. Kahn, *Adv. Mater.*, 2020, **32**, 2003482.
40 D. Macdonald, R. A. Sinton and A. Cuevas, *J. Appl. Phys.*, 2001, **89**, 2772–2778.
41 I. Levine, S. Gupta, A. Bera, D. Ceratti, G. Hodes, D. Cahen, D. Guo, T. J. Savenije, J. Ávila, H. J. Bolink, O. Millo, D. Azulay and I. Balberg, *J. Appl. Phys.*, 2018, **124**, 103103.
42 J. M. Harrowfield, B. W. Skelton and A. H. White, *J. Chem. Soc., Dalton Trans.*, 1993, 2011–2016.
43 Y. H. Chang, C. H. Park and K. Matsuishi, *J. Korean Phys. Soc.*, 2004, **44**, 889–893.
44 J. Endres, D. A. Egger, M. Kulbak, R. A. Kerner, L. Zhao, S. H. Silver, G. Hodes, B. P. Rand, D. Cahen, L. Kronik and A. Kahn, *J. Phys. Chem. Lett.*, 2016, **7**, 2722–2729.
45 S. R. Raga, Y. Jiang, L. K. Ono and Y. Qi, *Energy Technol.*, 2017, **5**, 1750–1761.
46 Lange's Handbook of Chemistry, 17th Edition, https://www.accessengineeringlibrary.com/browse/langes-handbook-of-chemistry-seventeenth-edition, accessed March 31, 2019.
47 Physical and thermodynamic properties of pure chemicals: data compilation (Continually updated resource, 1989) [WorldCat.org], https://www.worldcat.org/title/physical-and-thermodynamic-properties-of-pure-chemicals-data-compilation/oclc/19513328, accessed March 31, 2019.
48 Ammonia (7664-41-7) MSDS Melting Point Boiling Point Density Storage Transport, https://www.chemicalbook.com/ProductMSDSDetailCB9854275_EN.htm, (accessed March 26, 2019).
49 74-89-5 CAS MSDS (Methylamine) Melting Point Boiling Point Density CAS Chemical Properties, https://www.chemicalbook.com/ChemicalProductProperty_US_CB4387750.aspx, (accessed March 26, 2019).
50 J. Cazaux, *Appl. Surf. Sci.*, 2010, **257**, 1002–1009.
51 M. Nagoshi, T. Kawano and K. Sato, *Surf. Interface Anal.*, 2016, **48**, 470–473.
52 P. A. Anderson and A. L. Hunt, *Phys. Rev.*, 1956, **102**, 367–368.
53 H. P. Beck and G. Moretti, *Solid State Sci.*, 2020, **110**, 106359.
54 J. J. Uebbing and L. W. James, *J. Appl. Phys.*, 1970, **41**, 4505–4516.
55 M. R. Tubbs and A. J. Forty, *Br. J. Appl. Phys.*, 1964, **15**, 1553–1558.
56 D. Meggiolaro, S. G. Motti, E. Mosconi, A. J. Barker, J. Ball, C. A. R. Perini, F. Deschler, A. Petrozza and F. D. Angelis, *Energy Environ. Sci.*, 2018, **11**, 702–713.
57 J. Wiktor, F. Ambrosio and A. Pasquarello, *J. Mater. Chem. A*, 2018, **6**, 16863–16867.
58 M. H. Du, *J. Mater. Chem. A*, 2014, **2**, 9091–9098.
59 M.-H. Du, *J. Phys. Chem. Lett.*, 2015, **6**, 1461–1466.
60 A. Zohar, M. Kulbak, I. Levine, G. Hodes, A. Kahn and D. Cahen, *ACS Energy Lett.*, 2019, **4**, 1–7.
61 I. Levine, O. G. Vera, M. Kulbak, D.-R. Ceratti, C. Rehermann, J. A. Márquez, S. Levcenko, T. Unold, G. Hodes, I. Balberg, D. Cahen and T. Dittrich, *ACS Energy Lett.*, 2019, **4**, 1150–1157.
62 G. L. Breneman and R. D. Willett, *Acta Crystallogr., Sect. B: Struct. Crystallogr. Cryst. Chem.*, 1969, **25**, 1073–1076.
63 P. K. Bakshi, M. A. James, T. S. Cameron and O. Knop, *Can. J. Chem.*, 1996, **74**, 559–573.
64 M. E. Easton, A. J. Ward, B. Chan, L. Radom, A. F. Masters and T. Maschmeyer, *Phys. Chem. Chem. Phys.*, 2016, **18**, 7251–7260.
65 D. Schoemaker and A. Lagendijk, *Phys. Rev. B: Solid State*, 1977, **15**, 5927–5937.
66 W. Känzig and T. O. Woodruff, *J. Phys. Chem. Solids*, 1959, **9**, 70–92.
67 A. Lushchik, *Izv. Akad. Nauk Ehstonskoj SSR Fiz. Mat.*, 1980, **29**, 173–180.
68 B. V. R. Chowdari and N. Itoh, *J. Phys. Chem. Solids*, 1972, **33**, 1773–1783.
69 J.-H. Yang, W.-J. Yin, J.-S. Park and S.-H. Wei, *J. Mater. Chem. A*, 2016, **4**, 13105–13112.
70 O. Yaffe, Y. Guo, L. Z. Tan, D. A. Egger, T. Hull, C. C. Stoumpos, F. Zheng, T. F. Heinz, L. Kronik, M. G. Kanatzidis, J. S. Owen, A. M. Rappe, M. A. Pimenta and L. E. Brus, *Phys. Rev. Lett.*, 2017, **118**, 136001.
71 A. Marronnier, G. Roma, S. Boyer-Richard, L. Pedesseau, J.-M. Jancu, Y. Bonnassieux, C. Katan, C. C. Stoumpos,

M. G. Kanatzidis and J. Even, *ACS Nano*, 2018, **12**, 3477–3486.

72 A. M. A. Leguy, A. R. Goñi, J. M. Frost, J. Skelton, F. Brivio, X. Rodríguez-Martínez, O. J. Weber, A. Pallipurath, M. I. Alonso, M. Campoy-Quiles, M. T. Weller, J. Nelson, A. Walsh and P. R. F. Barnes, *Phys. Chem. Chem. Phys.*, 2016, **18**, 27051–27066.

73 A. V. Cohen, D. A. Egger, A. M. Rappe and L. Kronik, *J. Phys. Chem. Lett.*, 2019, **10**, 4490–4498.

74 Z. Andaji-Garmaroudi, M. Anaya, A. J. Pearson and S. D. Stranks, *Adv. Energy Mater.*, 2020, **10**, 1903109.

75 D. R. Ceratti, A. Zohar, R. Kozlov, H. Dong, G. Uraltsev, O. Girshevitz, I. Pinkas, L. Avram, G. Hodes and D. Cahen, *Adv. Mater.*, 2020, **32**(46), 2002467.

76 S. Sadhu, T. Buffeteau, S. Sandrez, L. Hirsch and D. M. Bassani, *J. Am. Chem. Soc.*, 2020, **142**(23), 10431–10437.

77 W. T. M. Van Gompel, R. Herckens, G. Reekmans, B. Ruttens, J. D'Haen, P. Adriaensens, L. Lutsen and D. Vanderzande, *J. Phys. Chem. C*, 2018, **122**, 4117–4124.

78 F. C. Schaefer, I. Hechenbleikner, G. A. Peters and V. P. Wystrach, *J. Am. Chem. Soc.*, 1959, **81**, 1466–1470.

79 B. Conings, S. A. Bretschneider, A. Babayigit, N. Gauquelin, I. Cardinaletti, J. Manca, J. Verbeeck, H. J. Snaith and H.-G. Boyen, *ACS Appl. Mater. Interfaces*, 2017, **9**, 8092–8099.

80 S. Shao, M. Abdu-Aguye, L. Qiu, L.-H. Lai, J. Liu, S. Adjokatse, F. Jahani, M. E. Kamminga, G. H. ten Brink, T. T. M. Palstra, B. J. Kooi, J. C. Hummelen and M. A. Loi, *Energy Environ. Sci.*, 2016, **9**, 2444–2452.

81 C. Zhao, B. Chen, X. Qiao, L. Luan, K. Lu and B. Hu, *Adv. Energy Mater.*, 2015, **5**, 1500279.

82 Z. Song, C. Wang, A. B. Phillips, C. R. Grice, D. Zhao, Y. Yu, C. Chen, C. Li, X. Yin, R. J. Ellingson, M. J. Heben and Y. Yan, *Sustainable Energy Fuels*, 2018, **2**, 2460–2467.

83 H. Syafutra, J.-H. Yun, Y. Yoshie, M. Lyu, S. N. Takeda, M. Nakamura, L. Wang and M.-C. Jung, *Nanomaterials*, 2020, **10**, 1253.

84 D. H. Jung, J. H. Park, H. E. Lee, J. Byun, T. H. Im, G. Y. Lee, J. Y. Seok, T. Yun, K. J. Lee and S. O. Kim, *Nano Energy*, 2019, **61**, 236–244.

85 Y. Rakita, I. Lubomirsky and D. Cahen, *Mater. Horiz.*, 2019, **6**, 1297–1305.

86 H. Tan, A. Jain, O. Voznyy, X. Lan, F. P. G. de Arquer, J. Z. Fan, R. Quintero-Bermudez, M. Yuan, B. Zhang, Y. Zhao, F. Fan, P. Li, L. N. Quan, Y. Zhao, Z.-H. Lu, Z. Yang, S. Hoogland and E. H. Sargent, *Science*, 2017, **355**, 722–726.

87 X. Tang, M. Brandl, B. May, I. Levchuk, Y. Hou, M. Richter, H. Chen, S. Chen, S. Kahmann, A. Osvet, F. Maier, H.-P. Steinrück, R. Hock, G. J. Matt and C. J. Brabec, *J. Mater. Chem. A*, 2016, **4**, 15896–15903.

88 F. Zu, T. Schultz, C. M. Wolff, D. Shin, L. Frohloff, D. Neher, P. Amsalem and N. Koch, *RSC Adv.*, 2020, **10**, 17534–17542.

89 S. Kim, S. Bae, S.-W. Lee, K. Cho, K. D. Lee, H. Kim, S. Park, G. Kwon, S.-W. Ahn, H.-M. Lee, Y. Kang, H.-S. Lee and D. Kim, *Sci. Rep.*, 2017, **7**(1), 1–9.

90 F. Ren, Z. Zhu, X. Qian, W. Liang, P. Mu, H. Sun, J. Liu and A. Li, *Chem. Commun.*, 2016, **52**, 9797–9800.

91 K. Mahmood, S. Sarwar and M. Taqi Mehran, *RSC Adv.*, 2017, **7**, 17044–17062.

